

## The CMS ECAL performance with examples

This content has been downloaded from IOPscience. Please scroll down to see the full text.

2014 JINST 9 C02008

(<http://iopscience.iop.org/1748-0221/9/02/C02008>)

View [the table of contents for this issue](#), or go to the [journal homepage](#) for more

Download details:

IP Address: 158.144.54.166

This content was downloaded on 16/01/2017 at 13:58

Please note that [terms and conditions apply](#).

You may also be interested in:

[CMS Electromagnetic Trigger commissioning and first operation experiences](#)

Pascal Paganini and the CMS collaboration

[Performance of the CMS electromagnetic calorimeter and its role in the hunt for the Higgs boson in the two-photon channel](#)

Federico De Guio and the CMS collaboration

[The CMS Electromagnetic Calorimeter: overview, lessons learned during Run 1 and future projections](#)

Cristina Biino

[Role of the CMS Electromagnetic Calorimeter in the hunt for the Higgs boson in the two-gamma channel](#)

T Tabarelli de Fatis and on behalf of the CMS Collaboration)

[Performance of calorimeters at the LHC](#)

Francesca Cavallari

[The CMS electromagnetic calorimeter barrel upgrade for High-Luminosity LHC](#)

Philippe Gras and the CMS collaboration

[Performance of CMS ECAL Preshower in 2007 test beam](#)

Syue-Wei Li, Apollo Go, Chia-Ming Kuo et al.

[Mitigation of Anomalous APD signals in the CMS Electromagnetic Calorimeter](#)

D A Petyt and the CMS collaboration)

[The CMS lead tungstate electromagnetic calorimeter](#)

R M Brown

13<sup>th</sup> TOPICAL SEMINAR ON INNOVATIVE PARTICLE AND RADIATION DETECTORS  
7–10 OCTOBER 2013  
SIENA, ITALY

## The CMS ECAL performance with examples

A. Benaglia<sup>1</sup>

*European Organization for Nuclear Research,  
CERN CH-1211, Genève 23, Switzerland*

*E-mail:* [andrea.benaglia@cern.ch](mailto:andrea.benaglia@cern.ch)

**ABSTRACT:** The electromagnetic calorimeter (ECAL) of the CMS experiment at the CERN Large Hadron Collider is a hermetic, fine grained, homogeneous calorimeter containing 75848 lead tungstate crystals, completed by a silicon preshower installed in front of the endcaps. The main characteristics of the ECAL are reviewed. These include the challenges of calibration and triggering in the LHC environment, as well as the reconstruction and identification of photons and electrons. Several results achieved by the CMS experiment particularly exploit the ECAL excellent performance, here illustrated with reference to specific examples, comprising the Higgs boson search and characterization in the  $H \rightarrow \gamma\gamma$  and  $H \rightarrow ZZ^{(*)}$  decay channels and the search for non-standard phenomena such as high-mass gauge bosons decaying into electrons and long-lived particles with delayed signals in the calorimeter.

**KEYWORDS:** Scintillators, scintillation and light emission processes (solid, gas and liquid scintillators); Scintillators and scintillating fibres and light guides; Calorimeters; Calorimeter methods

<sup>1</sup>For the CMS collaboration.

---

## Contents

<b>1</b>	<b>Introduction</b>	<b>1</b>
<b>2</b>	<b>The CMS ECAL</b>	<b>1</b>
2.1	The ECAL layout	1
2.2	The ECAL performance with test beam data	2
<b>3</b>	<b>The ECAL performance with collision data</b>	<b>3</b>
3.1	Triggering $e/\gamma$ candidates	3
3.2	Electromagnetic shower energy reconstruction and calibration	3
3.2.1	Channel inter-calibration	4
3.2.2	Time-dependent response changes	4
3.2.3	Energy corrections	5
3.3	Energy resolution	5
<b>4</b>	<b>Role of the ECAL in the discovery of the Higgs boson and the search for other phenomena</b>	<b>6</b>
4.1	Search for the SM Higgs boson in the $H \rightarrow \gamma\gamma$ channel	6
4.2	Search for the SM Higgs boson in the $H \rightarrow ZZ^{(*)} \rightarrow 4l$ channel	7
4.3	Search for new phenomena	9
<b>5</b>	<b>Conclusions</b>	<b>10</b>

---

## 1 Introduction

The Compact Muon Solenoid (CMS) experiment at the Large Hadron Collider (LHC) has a broad physics programme, including the investigation of the electroweak symmetry breaking mechanism through the direct search of the standard model (SM) Higgs boson, as well as the search for possible SM extensions. In this report, the instrumental and operational aspects of the CMS electromagnetic calorimeter (ECAL) relevant to the recent discovery of the Higgs boson [1] and in the search of non-standard, beyond-the-standard-model (BSM) phenomena are presented.

## 2 The CMS ECAL

### 2.1 The ECAL layout

The CMS ECAL [2, 3] is a compact, hermetic, fine-grain, homogeneous calorimeter made of 75848 lead tungstate ( $\text{PbWO}_4$ ) scintillating crystals. The choice of  $\text{PbWO}_4$  (density =  $8.28 \text{ g/cm}^3$ ) was primarily motivated by its radiation tolerance, its small radiation length ( $X_0 = 0.89 \text{ cm}$ ) and Molière radius ( $r_M = 2.19 \text{ cm}$ ), and its fast response (99% of the light is collected in 100ns, which is

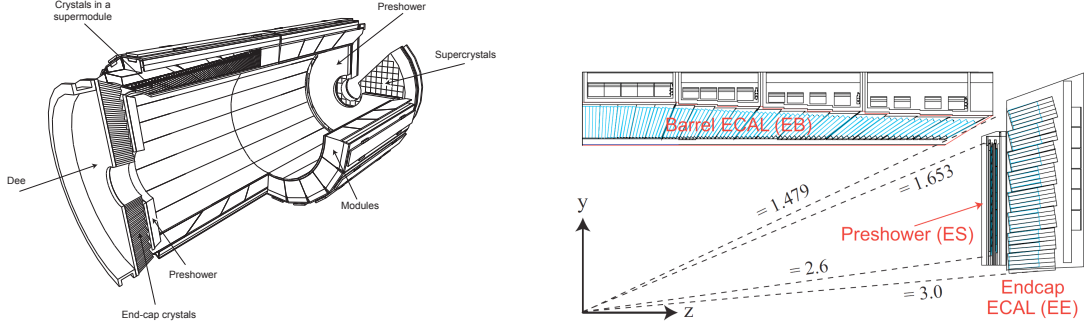


**Figure 1.** Schematic layout of the CMS electromagnetic calorimeter, presenting the arrangement of barrel supermodules, endcaps and the preshower in front (left). Geometric view of one quarter of the ECAL (right).

compatible with the 40 MHz interaction rate of the LHC). The crystals are arranged in a quasi-projective geometry and distributed in a central *barrel* section (EB) covering the pseudorapidity range  $|\eta| < 1.48$ , and two *endcaps* (EE) extending the coverage up to  $|\eta| = 3.0$ , as shown in figure 1. The barrel crystals are 23 cm long ( $\sim 26 X_0$ ) and have a front-face cross section of  $2.2 \times 2.2 \text{ cm}^2$ , while the endcap crystals are 22 cm long ( $\sim 25 X_0$ ), with a front-face cross section of  $2.86 \times 2.86 \text{ cm}^2$ . The crystal transverse size is comparable to the typical shower size in  $\text{PbWO}_4$ , which facilitates photon identification based on shower shape criteria. The main disadvantage of  $\text{PbWO}_4$  is its relatively low light yield, which requires the use of photodetectors with internal amplification inside the 3.8 T axial magnetic field of CMS. Silicon avalanche photodiodes (APDs, with an amplification factor of about 50) and vacuum phototriodes (VPTs, with an amplification factor of about 10) are used as photodetectors in the EB and EE respectively. The signal from the photodetectors is amplified and shaped by the front-end electronics, and then digitized at 40 MHz by a 12-bit analog-to-digital converter (ADC) on the front-end, providing a discrete set of amplitude measurements. These are stored in a buffer until a Level-1 (L1) trigger is received. At that time, the ten consecutive samples corresponding to the selected event are transmitted to the off-detector electronics for insertion into the CMS data stream. Knowing the typical pulse shape of each electronic channel, the signal amplitude ( $A$ ) can be reconstructed [4]. Moreover, ratios of sample amplitudes provide information about the timing of the signal with respect to the trigger [5]. A *preshower* detector (ES), composed of two layers of lead absorber ( $2 X_0$  and  $1 X_0$ ) instrumented with orthogonal layers of silicon strip sensors is placed in front of the endcaps ( $1.65 < |\eta| < 2.5$ ) to help with  $\pi^0/\gamma$  separation. Since the start of LHC operation, ECAL has run efficiently, with a small fraction (about 1% in EB, 2% in EE, and 3% in ES) of non-operational channels by the end of the first LHC running period (early 2013).

## 2.2 The ECAL performance with test beam data

The performance of the the calorimeter has been extensively tested with electron beams [6]. In a beam test setup with no magnetic field or inert material in front of the calorimeter, the ECAL barrel energy ( $E$ ) resolution has been measured to be

$$\frac{\sigma_E}{E} = \frac{2.8\%}{\sqrt{E[\text{GeV}]}} \oplus \frac{12\%}{E[\text{GeV}]} \oplus 0.3\%$$

for electrons impinging on the centre of the crystals. The electron energy was reconstructed as the sum of the energy deposits in a matrix of  $3 \times 3$  crystals around the impact point. The irreducible constant term, which dominates the energy resolution for high-energy electrons and photons, is affected by the non-uniformity of the longitudinal light collection, energy leakage from the back of the calorimeter, single-channel response uniformity and stability. In contrast to the beam test setup, additional contributions to the energy resolution are present in the real CMS environment. Material upstream of the ECAL can cause electron bremsstrahlung and photon conversions that affect all terms of the energy resolution. Moreover, residual miscalibrations of the channel-to-channel response and channel response changes with time due to radiation damage of the crystals and environmental instability impact on the constant term of the resolution. These effects have to be controlled to a fraction of a percent to maintain the excellent intrinsic resolution of ECAL.

### 3 The ECAL performance with collision data

#### 3.1 Triggering $e/\gamma$ candidates

Triggers for  $e/\gamma$  candidates are provided through the two-level trigger system of CMS. At Level-1, *trigger primitives* are formed at 40MHz from sums of the transverse energy ( $E_T$ ) measured by groups of crystals (e.g. arrays of  $5 \times 5$  crystals in EB). Coarse information on the lateral extent of the shower is provided by the front-end trigger electronics and exploited to suppress spurious triggers, such as those originated by direct ionization in the APD sensitive region [7]. This feature has allowed the single-photon L1 trigger to be operated at a low threshold of  $E_T = 20 \text{ GeV}$  in 2012. From offline data analysis, this trigger has been verified to be  $> 99\%$  efficient for  $E_T > 40 \text{ GeV}$ , providing full efficiency for the  $H \rightarrow \gamma\gamma$  search.

#### 3.2 Electromagnetic shower energy reconstruction and calibration

Electrons and photons deposit their energy over several ECAL crystals. Clusters of energy deposits are spread along the azimuthal direction due to the combined effect of secondary interactions in the tracker material (bremsstrahlung or photon conversions) and the 3.8T magnetic field of CMS. Dynamic clustering algorithms are used to merge clusters belonging to the same electromagnetic shower into so-called *superclusters* (SC) [8]. The best estimate of the  $e/\gamma$  candidate energy ( $E_{e/\gamma}$ ) is obtained from the sum of the signal amplitudes ( $A_i$ , in ADC counts) of the individual channels in the cluster, weighted with channel-dependent coefficients to correct for time response variations ( $S_i(t)$ ). The different channel responses are equalized by means of inter-calibration coefficients ( $C_i$ ) and calibrated by the ADC-to-GeV conversion ( $G$ ). Finally, imperfect clustering, material and geometry effects are accounted for ( $F_{e/\gamma}$ ). For endcap clusters the preshower energy ( $E_{ES}$ ) is also added. The full reconstruction equation is  $E_{e/\gamma} = F_{e/\gamma} \cdot [G \cdot \sum_i S_i(t) C_i A_i + E_{ES}]$  [9].

The effects of using the superclustering process and the application of  $F_{e/\gamma}$  corrections are shown in figure 2 for the invariant mass of  $e^+e^-$  pairs from Z decays, compared to a reconstruction based on a fixed cluster of  $5 \times 5$  crystals. The ratio of the energy in a fixed array of crystals to the uncorrected supercluster energy ( $E_{\text{raw}}$ ) is a convenient way to identify electrons with little bremsstrahlung in the tracker and photons which have not undergone conversions. For such particles, a better energy resolution is expected. To this purpose, the  $R_9 = E_{3 \times 3}/E_{\text{raw}}$  variable was introduced.

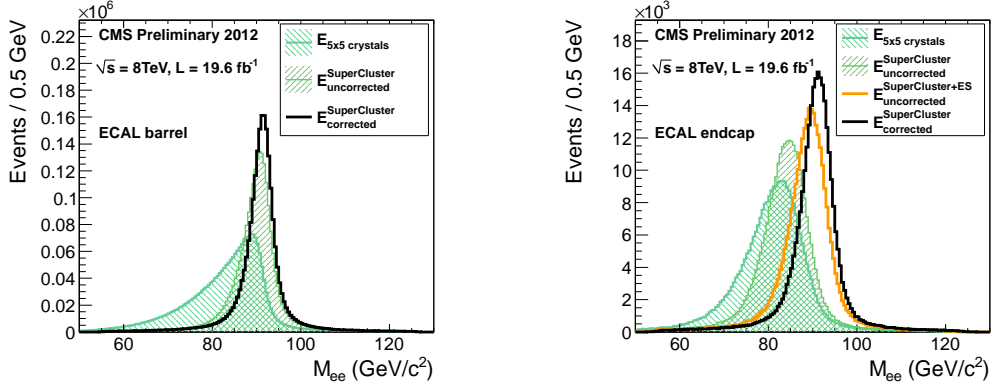


**Figure 2.** The impact on the  $Z \rightarrow e^+e^-$  energy scale and resolution for EB (left) and EE (right) from using clustering algorithms and cluster corrections to reconstruct the energy of the two electrons with respect to a reconstruction based on the sum of the bare energy deposits in a  $5 \times 5$  array of crystals.

### 3.2.1 Channel inter-calibration

The main sources of channel-to-channel response variation are the crystal intrinsic light yield variation of  $\sim 15\%$  and the gain spread of the photodetectors in EE of  $\sim 25\%$ . Calibrations from laboratory measurements and crystal exposure to cosmic rays have provided an acceptable performance at startup [10]. More refined calibration procedures have been used *in situ* exploiting different properties of collision events [9]. These include  $\phi$ - and time-invariance of the energy flow in crystals at a given pseudorapidity in minimum-bias events, the  $\pi^0/\eta$  mass constraint on the energy of the two photons from their decay into photon pairs, and the momentum constraint on the energy of isolated electrons from W and Z decays. For the first two methods, dedicated high-rate ( $\sim 5$  kHz) trigger streams have been developed. These identify, online, interesting ECAL regions and provide limited data in the region of the photon candidates within the allocated CMS trigger bandwidth. The residual mis-calibration after the combination of the three methods contributes less than  $\sim 0.4\%$  to the constant term of the resolution in the central EB ( $|\eta| < 1$ ) and less than  $\sim 2\%$  in most of the EE.

### 3.2.2 Time-dependent response changes

At a working temperature of  $18^\circ\text{C}$ , the temperature dependence of the crystal light yield ( $-2\%/^\circ\text{C}$ ) and APD gain ( $-2.3\%/^\circ\text{C}$ ) require an accurate temperature stabilization (better than  $0.05^\circ\text{C}$  in EB and  $0.1^\circ\text{C}$  in EE), which is ensured by a water cooling system. The contribution of temperature and gain fluctuations to the energy resolution is below  $0.2\%$ . The stability of the bias voltage supplies has also met specifications [11].

In the harsh radiation environment of LHC, while the scintillation mechanism of  $\text{PbWO}_4$  stays unaffected, the crystal transparency changes in a dose-rate dependent way. At the ECAL operating temperature, the crystal transparency is recovered. The result is a cycle of transparency changes between LHC collision runs and machine refills. A monitoring system [12] based on the injection of laser light at  $\lambda = 440\text{nm}$  (close to  $\text{PbWO}_4$  emission peak) into each crystal is used to track and correct for these variations during LHC operations. The variation of the ECAL response to laser light throughout 2011 and 2012 runs is shown in figure 3 left. The observed transparency

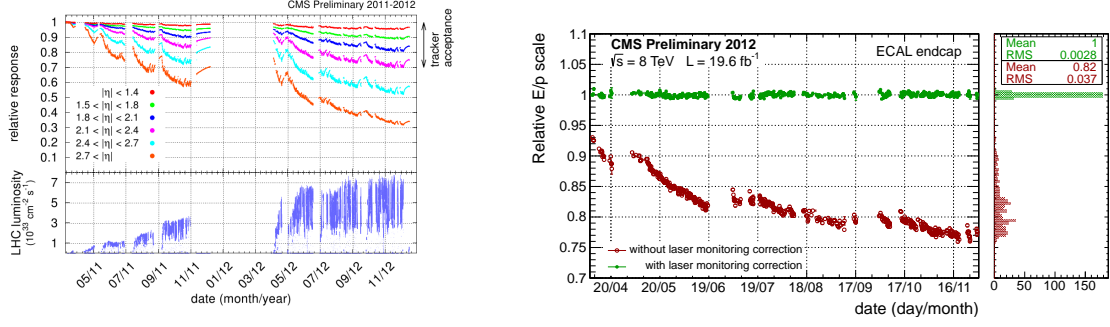


**Figure 3.** ECAL relative response to the laser monitoring system in 2011 and 2012. The response is averaged over the pseudorapidity ranges listed in the legend. Periods with no data correspond to LHC technical stops (left). Stability of the ECAL relative response in physics events during the 2012 run for electrons from W decays in the endcap, upon application of laser monitoring corrections — green dots. Uncorrected data are also shown — red dots (right).

losses are consistent with expectations and reach up to 6% in EB and 30% in EE at the end of the CMS acceptance region for  $e/\gamma$  at  $|\eta| = 2.5$ . Laser measurements are made on each ECAL crystal every  $\sim 40$  minutes. This enables correction factors  $S_i(t)$  to be delivered in less than 48h for prompt reconstruction of CMS data. The overall stability of the energy reconstruction, upon the application of the laser monitoring corrections, is checked using the three methods described above for inter-calibration purposes. In figure 3 right, one such example is shown using electrons from W decays. A stability rms of about 0.1% and 0.3% was achieved for EB and EE respectively. The ECAL response over time is also modified by some  $\eta$ -dependent radiation-induced effects. The APD leakage current increase, due to silicon bulk damage, causes a slow increase in noise. VPT photocathode conditioning causes response losses of  $\sim 20\%$  and is not disentangled from the  $\text{PbWO}_4$  transparency variations with the laser monitoring system.

### 3.2.3 Energy corrections

Particle-level energy corrections  $F_{e/\gamma}$  are applied on top of calibrated clusters to account for the effects of the material upstream of the ECAL as well as local shower containment effects and other geometrical and particle-dependent factors. Corrections have been derived separately for electrons and photons by means of a Monte-Carlo-driven multivariate analysis (MVA). Input variables include shower shape information, the shower position within the ECAL and in CMS, and global event variables sensitive to pileup. Energy corrections closely follow the distribution of the material budget in front of the ECAL, shown in figure 4 left. They are sizable and are up to 6%/10% for low/high showering electrons in the pseudorapidity region  $1 < |\eta| < 2$ , where the tracker material has a thickness of  $\sim 2 X_0$  equivalent.

### 3.3 Energy resolution

The energy resolution achieved with fully calibrated and corrected superclusters has been compared between collision data and Monte Carlo simulation. The ECAL response in the simulation is tuned to match beam test results, including a detailed description of the single channel noise, single-channel response spread corresponding to the estimated residual mis-calibration, and a constant



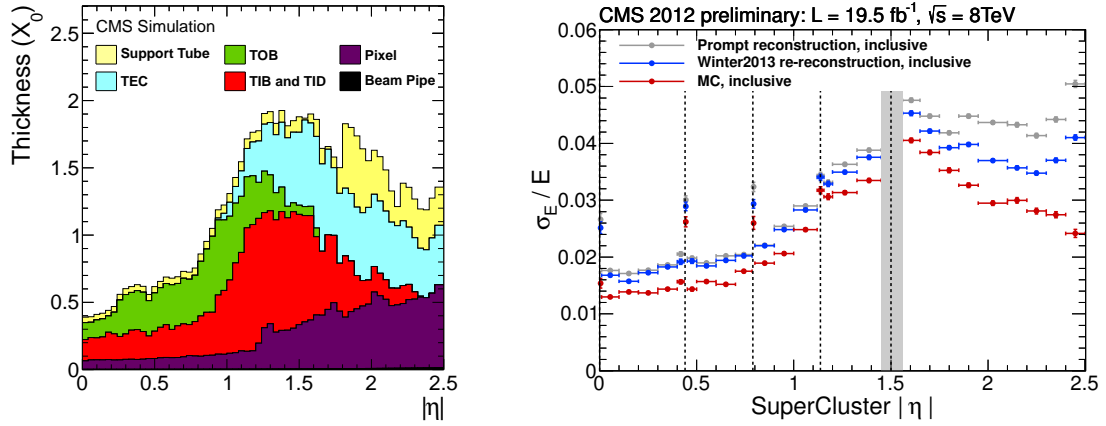


**Figure 4.** Amount of material (in units of radiation lengths) upstream of the ECAL (left). Electron energy resolution as a function of pseudorapidity for electrons from  $Z \rightarrow e^+e^-$  decays. In red, the energy resolution estimated on Monte Carlo events is shown, while in blue and gray the resolution for respectively promptly-reconstructed data and a later reconstruction of the same data sample upon the usage of the best calibrations available are shown (right).

term of 0.3%. The few non-operational channels are also simulated. The electron energy resolution is estimated from the  $Z \rightarrow e^+e^-$  peak width by means of an unbinned maximum likelihood fit<sup>1</sup> to the invariant mass distribution of  $e^+e^-$  pairs. The energy scale and resolution of each electron is allowed to float in the fit. The results are obtained in bins of  $|\eta|$ . Figure 4 right shows the energy resolution obtained in the central barrel ( $|\eta| < 1$ ), which is around 1.7% for all electrons from  $Z$  decays. The impact of the material upstream of the ECAL is particularly relevant for  $|\eta| > 1$ . Especially in the endcaps, a re-reconstruction of the data sample with improved calibrations, with respect to those used for CMS prompt data reconstruction, provides a sizable improvement in the resolution. There is nevertheless a residual difference between data and simulation. The most likely contributions come from the limited precision of the single channel calibration and cluster corrections for material effects. In order for the Monte Carlo to match the observed resolution in data, an extra smearing term is added to the constant term of the energy resolution in the simulation. This approach provides a conservative estimate of resolution at high energies.

## 4 Role of the ECAL in the discovery of the Higgs boson and the search for other phenomena

### 4.1 Search for the SM Higgs boson in the $H \rightarrow \gamma\gamma$ channel

The distinctive experimental signature of the  $H \rightarrow \gamma\gamma$  decay mode is a narrow peak in the invariant mass distribution from two isolated photons of high transverse momentum, over a large background from irreducible QCD di-photon production and reducible  $\gamma$ +jet or di-jet production with jets faking photons. For a light Higgs boson ( $m_H \lesssim 150\text{GeV}$ ), the resolution of the reconstructed invariant

<sup>1</sup>The invariant mass distribution is modeled with a Breit-Wigner function of mass  $m_Z = 91.188\text{GeV}$  and width  $\Gamma_Z = 2.495\text{GeV}$  convoluted with a Gaussian response function of width  $\sigma_m$ , with  $\sigma_m/m = \sigma_{E_1}/E_1 \oplus \sigma_{E_2}/E_2$ .



mass is completely determined by instrumental effects, namely

$$\frac{\sigma_{m_{\gamma\gamma}}}{m_{\gamma\gamma}} = \frac{1}{2} \left( \frac{\sigma_{E_{\gamma_1}}}{E_{\gamma_1}} \oplus \frac{\sigma_{E_{\gamma_2}}}{E_{\gamma_2}} \oplus \frac{\sigma_{\vartheta_{\gamma\gamma}}}{\tan \frac{\vartheta_{\gamma\gamma}}{2}} \right).$$

The first two terms represent the energy resolution for the two photons. The last term is the resolution for the opening angle between the two photons, derived from the positions of the showers and the interaction vertex. This term is mostly determined by the identification of the correct interaction vertex.<sup>2</sup> The correct vertex is chosen by means of a MVA technique that uses the kinematic properties of the tracks associated with each vertex and their correlation with the di-photon system as input variables. The Higgs invariant mass resolution is estimated from the simulation, introducing the photon energy resolution and correct-vertex-finding probability measured with data. Due to the progress in clustering and calibration, the mass resolution has shown a continued improvement over time — from  $\sim 1.5\%$  for all photon classes on 7 TeV data to  $\sim 1.1\%$  on the same dataset with the most up-to-date calibrations. For the 8 TeV dataset, still largely based on promptly-reconstructed data, the mass resolution for the full photon ensemble is  $\sim 1.3\%$ . A 5 – 10% improvement is expected upon the application of updated calibration and energy corrections. For the best photon class (unconverted, central barrel, high- $p_T$  photons), it is already  $\sim 1\%$ , as shown in figure 5 left.

In addition to excellent mass resolution, a crucial aspect for the analysis is an effective photon identification, made possible by the high ECAL granularity. Several variables are combined into a MVA discriminator to distinguish photons from  $\pi^0$  and jet fragments. Among them, the transverse spread of the electromagnetic shower and isolation variables based on the tracker, ECAL and hadron calorimeter measurements play a major role.

The most powerful analysis approach uses a MVA technique to split di-photon candidates into four categories based on photon, vertex, and global event variables, giving more weight to unconverted photon candidates with good mass resolution and signal-to-background ratio. Exclusive categories are also formed to enhance the analysis sensitivity to vector boson fusion and associated Higgs production modes, and to improve the precision of the measurement of the Higgs couplings to fermions and vector bosons. In each category, the background is estimated from data with a parametric fit to the invariant mass spectrum of the di-photon candidates. The combined result of all the categories in the 7 and 8 TeV data samples is the observation of an excess around 125 GeV, with a local significance of  $3.2\sigma$ , as visible in figure 5 right [13].

#### 4.2 Search for the SM Higgs boson in the $H \rightarrow ZZ^{(*)} \rightarrow 4l$ channel

The  $H \rightarrow ZZ^{(*)} \rightarrow 4l$  decay mode, analyzed in its  $4e$ ,  $4\mu$ , and  $2e2\mu$  final states, is characterized by a narrow peak over a very low and well-defined background. For a  $\sim 125$  GeV Higgs boson, the softest of the four leptons has a  $p_T$  well below 15 GeV (as visible in figure 6 left). The analysis depends critically on the capability of detecting leptons down to very low  $p_T$  values. For electrons, this is a difficult kinematic region due to bremsstrahlung radiation in the 3.8 T magnetic field. Electrons are efficiently reconstructed and identified down to  $p_T = 7$  GeV by combining the tracker

<sup>2</sup>In 2012, about 20 interaction vertices are reconstructed for each event, with a rms spread of 6 cm along the beam axis. The vertex must be located to better than 1 cm to make a negligible contribution to the mass resolution, as compared to the energy resolution.

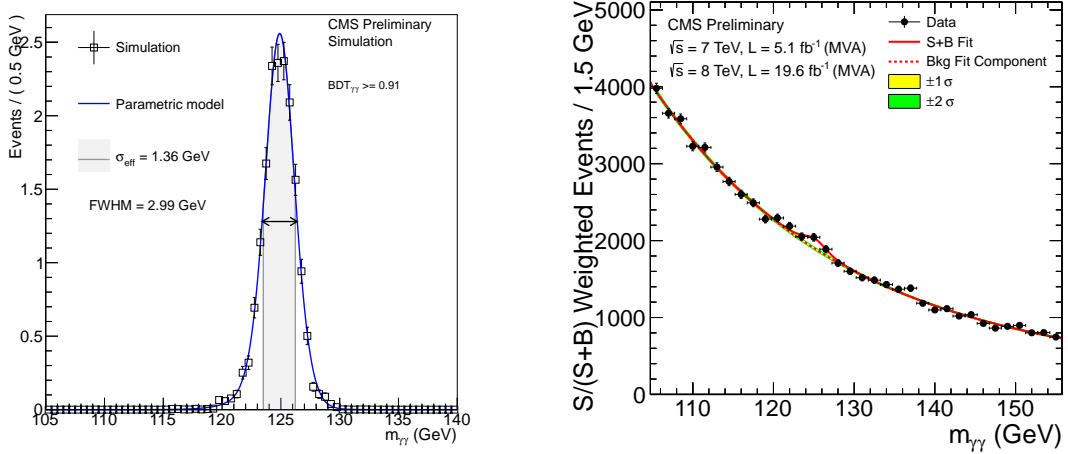


**Figure 5.** Invariant mass distribution for a Higgs of  $m_H = 125 \text{ GeV}$  decaying into two photons for the best-resolution category (left). The di-photon invariant mass distribution for the combination of all analysis categories, adding together the 7 and 8 TeV datasets. Each event is weighted by the  $S/(S+B)$  value of its category. The lines represent the background and signal+background parametric models fitted to the data (right).

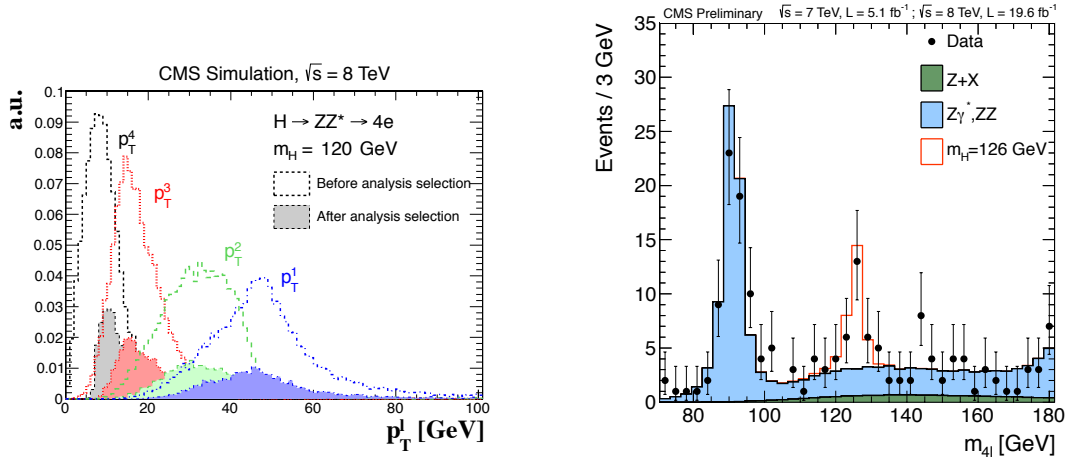


**Figure 6.** Transverse momentum distribution for each of the four leptons (ordered in  $p_T$ ) from  $H \rightarrow ZZ^{(*)} \rightarrow 4l$  signal events and for a mass hypothesis of  $m_H = 120 \text{ GeV}$ . The distributions are obtained using Monte Carlo signal samples and shown at generator level within  $\eta$  acceptance (empty histograms), and for selected events (shaded histograms) in the  $4e$  channel (left). Distribution of the observed  $4l$  invariant mass for the sum of  $4e$ ,  $4\mu$ , and  $2e2\mu$  channels over the full 2011 and 2012 datasets (right).

and the ECAL measurements to improve the energy resolution at low  $p_T$ . The approach for electron identification is similar to that for photons, with the additional requirement of matching the ECAL supercluster with an electron track in terms of location and momentum. The excess of events observed by this analysis around  $126 \text{ GeV}$ , combining the three final states, is shown in figure 6 right and corresponds to a local significance above the expected background of almost  $7\sigma$  [14].

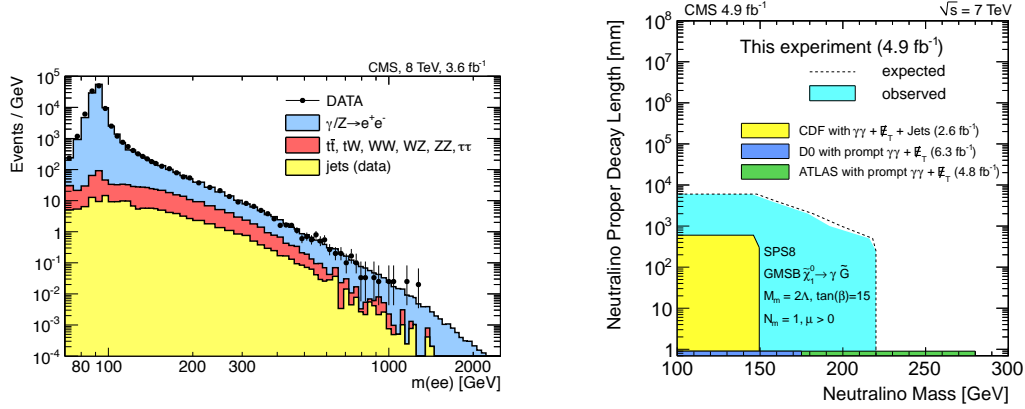


**Figure 7.** The invariant mass spectrum of di-electron events for the 8 TeV dataset in the search for a narrow  $Z'$  resonance (left). The observed exclusion region for the mass and proper decay length of the  $\tilde{\chi}_1^0$  neutralino in a GMSB supersymmetry model (right).

### 4.3 Search for new phenomena

New heavy gauge bosons are predicted by various scenarios of physics beyond the standard model. In the simplest SM extensions,  $W'$  and  $Z'$  bosons are expected to appear as narrow resonances with decay modes and branching fractions similar to those of ordinary  $W$  and  $Z$  bosons. Decay channels into lepton pairs are therefore the most promising to study. The same final states are also predicted by many other models for new physics. Focusing on final states with electrons ( $e\nu_e$  or  $e^+e^-$ ), it is crucial that the ECAL be able to reconstruct and measure electron energies up to the TeV region. This is a very different regime from that of Higgs boson searches. The good performance of the calorimeter can be deduced from figure 7 left, where the di-electron invariant mass spectrum is shown. The Monte Carlo well describes the whole observed data spectrum, with no significant excess of events observed. The same conclusions can be derived for electron-neutrino searches. Interpreting the  $e\nu_e/e^+e^-$  final states in terms of a heavy  $W'/Z'$  with SM couplings, masses below 2.90 TeV/2.59 TeV can be excluded by combining the results from the electron and the muon channels. The contributions to the analysis from both channels are almost the same [15, 16].

Another interesting study that exploits the CMS ECAL is the search for new, heavy particles with long lifetimes, predicted in many BSM models such as supersymmetry (SUSY) with gauge-mediated supersymmetry breaking (GMSB). At the LHC, a GMSB benchmark scenario could manifest itself with the production of a pair of neutralinos,  $\tilde{\chi}_1^0$ , which are the next-to-lightest supersymmetric particles in this model, and can be long-lived. These, in turn, could decay into a photon and an undetectable gravitino. The final state would then be characterized by the presence of missing transverse energy and two photons reaching the detector at a later time than the prompt, relativistic particles produced at the interaction point. The search for a long-lived neutralino in CMS is based on a novel technique that exploits the excellent time measurement provided by the ECAL.<sup>3</sup> The time measurement is the energy-weighted mean time for the crystals within the cluster associated with a photon candidate (see section 2.1). With no excesses observed in this search, an added bonus of the timing information is that simultaneous limits on the neutralino mass and proper decay length can be set, as shown in figure 7 right [17].

<sup>3</sup>With  $Z \rightarrow e^+e^-$  events, a time resolution in data of  $\sim 190$  ps in EB and  $\sim 280$  ps in EE is measured.

## 5 Conclusions

The CMS ECAL has efficiently operated for two years at the LHC, meeting the design specifications. The energy resolution obtained is constantly improving, thanks to the hard work to better understand systematic effects, such as local containment fluctuations and the effects of upstream material. The excellent ECAL performance was crucial for the discovery of a Higgs boson in CMS, particularly in the  $H \rightarrow \gamma\gamma$  and  $H \rightarrow ZZ^{(*)} \rightarrow 4l$  channels. Data from the ECAL have enabled electrons and photons to be reconstructed up to the TeV scale. This is fundamental for the many searches of non-standard and new phenomena beyond the standard model.

## References

- [1] CMS collaboration, *Observation of a new boson with mass near 125 GeV in pp collisions at  $\sqrt{s} = 7$  and 8 TeV*, *JHEP* **06** (2013) 081 [[arXiv:1303.4571](#)].
- [2] CMS collaboration, *The CMS experiment at the CERN LHC*, 2008 *JINST* **3** S08004.
- [3] CMS collaboration, *The CMS electromagnetic calorimeter project: Technical Design Report*, CERN-LHCC-97-33 (1997).
- [4] P. Adzic et al., *Reconstruction of the signal amplitude of the CMS electromagnetic calorimeter*, *Eur. Phys. J. C* **46** (2006) 23.
- [5] CMS collaboration, *Time Reconstruction and Performance of the CMS Electromagnetic Calorimeter*, 2010 *JINST* **5** T03011 [[arXiv:0911.4044](#)].
- [6] P. Adzic et al., *Energy resolution of the barrel of the CMS electromagnetic calorimeter*, 2007 *JINST* **2** P04004.
- [7] CMS collaboration, D.A. Petyt, *Anomalous APD signals in the CMS Electromagnetic Calorimeter*, *Nucl. Instrum. Meth. A* **695** (2012) 293.
- [8] CMS collaboration, *CMS Physics: Technical Design Report, Volume 1: Detector Performance and Software*, CERN-LHCC-2006-001 (2006).
- [9] CMS collaboration, *Energy calibration and resolution of the CMS electromagnetic calorimeter in pp collisions at  $\sqrt{s} = 7$  TeV*, 2013 *JINST* **8** P09009 [[arXiv:1306.2016](#)].
- [10] CMS ELECTROMAGNETIC CALORIMETER GROUP collaboration, P. Adzic et al., *Intercalibration of the barrel electromagnetic calorimeter of the CMS experiment at start-up*, 2008 *JINST* **3** P10007.
- [11] CMS collaboration, *Performance and Operation of the CMS Electromagnetic Calorimeter*, 2010 *JINST* **5** T03010 [[arXiv:0910.3423](#)].
- [12] M. Anfreville et al., *Laser monitoring system for the CMS lead tungstate crystal calorimeter*, *Nucl. Instrum. Meth. A* **594** (2008) 292.
- [13] CMS collaboration, *Updated measurements of the Higgs boson at 125 GeV in the two photon decay channel*, CMS-PAS-HIG-13-001 (2013).
- [14] CMS collaboration, *Properties of the Higgs-like boson in the decay  $H \rightarrow ZZ \rightarrow 4l$  in pp collisions at  $\sqrt{s} = 7$  and 8 TeV*, CMS-PAS-HIG-13-002.
- [15] CMS collaboration, *Search for new physics in final states with a lepton and missing transverse energy in pp collisions at the LHC*, *Phys. Rev. D* **87** (2013) 072005 [[arXiv:1302.2812](#)].
- [16] CMS collaboration, *Search for heavy narrow dilepton resonances in pp collisions at  $\sqrt{s} = 7$  TeV and  $\sqrt{s} = 8$  TeV*, *Phys. Lett. B* **720** (2013) 63 [[arXiv:1212.6175](#)].
- [17] CMS collaboration, *Search for long-lived particles decaying to photons and missing energy in proton-proton collisions at  $\sqrt{s} = 7$  TeV*, *Phys. Lett. B* **722** (2013) 273 [[arXiv:1212.1838](#)].